Chemical Science

EDGE ARTICLE

View Article Online
View Journal | View Issue

Cite this: *Chem. Sci.*, 2014, **5**, 1493

Computational prediction and experimental confirmation of B-site doping in $YBa_2Fe_3O_8$†

Christopher Collins,[a] Matthew S. Dyer,[a] Antoine Demont,[a] Philip A. Chater,[a] Michael F. Thomas,[b] George R. Darling,[a] John B. Claridge[a] and Matthew J. Rosseinsky*[a]

Received 30th September 2013
Accepted 24th December 2013

DOI: 10.1039/c3sc52734d

www.rsc.org/chemicalscience

In this work we use calculations to obtain reaction enthalpies for the formation of $YBa_2Fe_{3-x}M_xO_8$ (where M = Co, Ni and Mn and $x = 1$, 2 and 3) from binary oxides and oxygen gas using Density Functional Theory (DFT). Based upon these calculations we are able to make predictions on favourable levels of doping and B-site ordering for $YBa_2Fe_{3-x}M_xO_8$, followed by experimental investigation in the same study. The composition where we predict doping to be favourable was experimentally investigated and a triple perovskite is found to be the major phase, confirming the prediction. Optimisation of the synthesis produced a phase-pure triple perovskite, $Y_{1.175}Ba_{1.825}Fe_2MnO_{8\pm\delta}$, formed in a narrow compositional window. The crystal structure of this phase was analysed using Powder X-ray Diffraction (PXRD), iodometric titrations, Mössbauer spectroscopy and Neutron Powder Diffraction (NPD). This is the first reported example of ordered or disordered Fe and Mn coexistence in this structure type. We compare the observed structure against the initial DFT predictions and find them to be in good agreement and conclude that the computational methods presented within this work can be used as a predictive guide to the synthesis of oxide materials.

Introduction

The properties of transition metal oxides are controllable by substitution at the metal sites. When several candidate sites are available, qualitative crystal chemical considerations may not always be capable of predicting the outcome of a substitution reaction. Here we explore the use of *ab initio* calculations to define the outcome of site substitution in an ordered triple perovskite.

Complex metal oxides are important scientifically because of their structural diversity and the wide range of novel phenomena they sustain, including charge ordering, colossal magnetoresistance and multiferroic behaviour. They have applications in many industrial and technological areas including catalysis,[1] solid oxide fuel cell (SOFC)[2] electrolytes and electrodes, transparent conductors,[3] superconductors,[4] ferro- and piezoelectrics,[5] dielectric materials,[6] thermoelectrics,[7] positive temperature co-efficient of resistivity materials (PTCR)[8] and ferrite permanent magnets.[9] Substitution into a parent structure permits property tuning in all of these application classes – examples are the evolution of the d.c. conductivity and area specific resistance (ASR) in the $Ba_{1-x}Sr_xFe_{1-y}Co_yO_{3-\delta}$[10–13] family of SOFC cathode materials, and band gap and resistivity tuning in the doped ZnO[14–16] family of transparent conducting oxides.

The structure of the superconductor $YBa_2Cu_3O_7$ (ref. 17) is based upon the ABO_3 perovskite structure that is extended to form a three-fold super structure in the *c*-axis direction, hereafter referred to as a $3a_p$ structure. $YBa_2Fe_3O_8$ (ref. 18) (Fig. 1a) was the first $3a_p$ analogue of the superconductor $YBa_2Cu_3O_7$ in

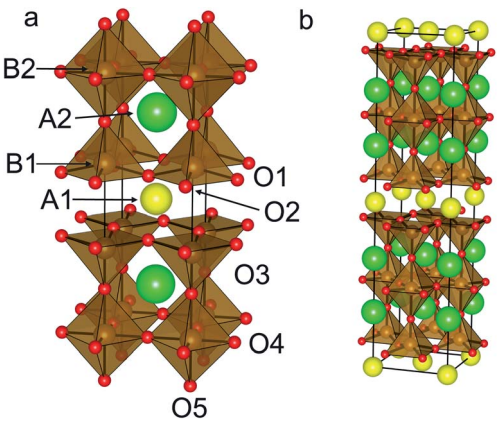

Fig. 1 (a) Reported structure for $YBa_2Fe_3O_8$, including the atomic labels used in this study. With tetragonal symmetry O1 and O2 are equivalent. (b) ($a + b$, $a - b$, $2c$) super-cell used in DFT calculations. Atoms coloured as follows: Y (yellow), Ba (green), Fe (brown) and O (red).

[a]*Department of Chemistry, University of Liverpool, Crown Street, Liverpool, L69 7ZD, UK. E-mail: rossein@liv.ac.uk*

[b]*Department of Physics, University of Liverpool, Liverpool, L69 7ZE, UK*

† Electronic supplementary information (ESI) available. See DOI: 10.1039/c3sc52734d

which Cu was fully replaced by another transition metal, and hence has been the object of considerable study.[18–23] It is a good candidate for predictive substitution as it is related to a number of other functional oxide materials in terms of system size,[17,24] structural motif[17,25] and some of the elements included in the system have been previously reported in other functional systems.[10,17,25] Long range ordering in the *c* direction is driven by ordering of oxygen vacancies (one ninth per triple perovskite ($A_3B_3O_9$) Formula Unit (FU)). These ordered vacancies create distinct A- and B-site environments within the structure. There are three A-sites, one hosting Y^{3+} ions co-ordinated to eight O^{2-} ions and two Ba sites co-ordinated to twelve O^{2-} ions. The B-sites are five co-ordinate square based pyramids and six co-ordinate octahedral sites, both distorted away from ideal polyhedral geometry: the octahedral site has four short and two long bonds, and the square pyramidal site has one short and four long bonds. $YBa_2Fe_3O_8$ orders antiferromagnetically at ~700 K (ref. 20–22) with a G-type magnetic structure.[23]

In this work we explore the use of Density Functional Theory (DFT) to guide the synthesis of B-site doped $YBa_2Fe_3O_8$.[18] While previous reports exist for substitution of Co into the $YBa_2Fe_3O_8$ compound,[19] substitution with Ni or Mn is currently unreported. This allows for both the validation of the computational method for the system by calculating Co substitution and for the prediction of unreported substitutions. Irrespective of the A-site composition, no compounds containing Fe and Mn have been previously reported in this structure.

Given the multiplicity of possible sites for doping, it is not trivial to identify where a substitution will take place. Prediction of whether a dopant will favour one of the available B-site geometries by looking at known structures is not reliable as precedents exist for doping at each of the sites found in the $3a_p$ structure.[26–28] It is also possible that B-site doping may occur in a disordered fashion over both B-sites. Given the widespread applicability of doped metal oxides it is highly desirable to use calculations to aid in predicting how to substitute the compound in order to reduce the number of syntheses that are required to find new compounds.

The calculation of stable levels of doping in $YBa_2Fe_3O_8$ is a complex computational problem because of the number of metal species present and two different chemical environments for Fe^{3+}. The prediction of ionic substitution based on a database of structures has been reported previously.[29] It has also been shown that all unique configurations of a structure can be generated using symmetry, and the most stable configuration determined by calculating relative energies between configurations.[30] This method has been applied in calculating the solid solutions of some binary and ternary oxides[31–33] and carbonate systems[34,35] and for a number of other system types.[36–38] Convex hull calculations have also been previously used in the prediction and synthesis of compounds with some success,[39] however the construction of convex hulls for systems containing four or more elements is impractical.

The complex structures of many functional transition metal oxides require large numbers of potential disordered configurations to be investigated in an exhaustive study. For example the largest super-cell used here for the composition $YBa_2Fe_2MnO_8$ has 16 Fe atoms and 8 Mn atoms distributed over 24 B-sites. Ignoring symmetry, there are 24!/16!8! = 735 471 ways of arranging these atoms, which reduces to 24 371 configurations not related by symmetry. Since such an exhaustive approach is clearly unfeasible in this case, we propose a more practical, simplified model. Previously it has been shown that DFT calculations can be configured to closely reproduce experimental reaction enthalpies for previously known perovskite materials, such as the $LaMO_3$ system, where M indicates a transition metal species[40,41] for calculations performed at 0 K. This work utilises the capability of DFT to calculate formation energies from binary oxides as a predictive tool, and is demonstrated in a system containing four different cation species and covering three different dopants with a range of doping levels.

We begin by calculating an energy of M substitution for doped $YBa_2Fe_{3-x}M_xO_8$ in a selected number of B-site configurations, representative of the possible orderings. We then experimentally test the following hypothesis: when this substitution energy is negative, doping will be experimentally favourable and conversely when the substitution energy is positive, doping would be unfavourable. We demonstrate the methodology for $YBa_2Fe_{3-x}M_xO_8$ when M = Co which has previously been synthesised[19] and then make predictions for doping when M = Mn and Ni.

Reaction energies

We start our calculation of reaction enthalpies by defining the dopant species M* by the binary oxide of M and a required amount of O_2 gas required to balance any change in the charge state of M in the doped compound to the 3+ oxidation state:

$$M^* = \left(\frac{x}{2}Mn_2^{3+}O_3\right), \left(\frac{x}{3}Co_3^{2.67+}O_4 + \frac{x}{12}O_2\right), \left(xNi^{2+}O + \frac{x}{4}O_2\right) \quad (1)$$

For reference calculations of the energies of binary oxides, the initial atomic coordinates and unit cells were used as reported in the literature.[42–47] Where multiple possible binary oxides are reported for the transition metals (M = Co and Mn) the oxide which gave an overall charge state as close to 3+ as possible was selected in order to minimise the amount of O_2 required to balance the equation. When M = Mn, no change in formal oxidation state is required, for M = Co and Ni, we assume that all of the M atoms increase their average oxidation state to be formally 3+ as this is reported experimentally for Co in this system.[19]

A substitution energy, ΔE_{sub}, can then be defined for the formation of the doped material from the undoped parent, binary oxides and gas phase oxygen where required (Eqn (2)).

$$YBa_2Fe_3O_8 - \frac{x}{2}Fe_2O_3 + M^* \xrightarrow{\Delta E_{sub}} YBa_2Fe_{3-x}M_xO_8 \quad (2)$$

The most favoured configuration at each doping level is defined as the composition that yields the lowest substitution energy, ΔE_{sub}. A negative value of ΔE_{sub} is used across doping species and doping levels to predict that doping is likely to be

possible. The energy ΔE_{sub} is closely related to other potentially relevant reaction energies, as discussed in the ESI.†

Since we are calculating energies at each end of the solid solution and values in between, we can also calculate energies relative to an ideal solid solution. Particularly stable compositions might be expected to have energies that lie below the energy of the ideal solid solution. Alternatively increases in energy indicate that the solid solution is unfavourable as has been suggested for solid solutions between binary materials,[48] which could suggest that phase separation is likely. For our systems, a solid-solution energy, ΔE_{SS}, is calculated according to Eqn (3):

$$(1-x)YBa_2Fe_3O_8 + xYBa_2M_3O_8 \xrightarrow{\Delta E_{SS}} YBa_2Fe_{3-x}M_xO_8 \quad (3)$$

In the system examined in this work the $YBa_2M_3O_8$ end members of the solid solutions are not reported in ordered $3a_p$ structures (although $YBa_2Co_3O_{8+\delta}$ is reported as a disordered cubic perovskite[49]), and so the solid-solution energy is not a true prediction of phase stability (competing phase separation into the two ordered end members cannot occur experimentally). Instead we use ΔE_{sub} (Eqn (2)) for our predictions of the outcomes of substitution reactions (Fig. 3a). However, for clarity in identifying the differences between configurations at each value of x we have used ΔE_{SS} (Eqn (3) and Fig. 3b–d).

Doping models

The initial atomic coordinates and unit cell for the calculations were taken from the reported crystal structure of $YBa_2Fe_3O_8$ in an $(a + b, a - b, 2c)$ super-cell of the nuclear cell (Fig. 1b).[18] This super-cell allows calculations for G-type antiferromagnetic and ferromagnetic ordering, and contains four octahedral and eight square pyramidal B-sites, over which the various transition metal cations were distributed at each level of doping.

The different B-site configurations considered for different doping levels are shown in Fig. 2. For full substitution ($x = 3$) only one B-site configuration is possible. For $x = 1$ and 2, three different B-site configurations were considered in order to be able to approximate the site preferences of the dopant species. In the first configuration, which we named "Octahedral", octahedral sites are preferred for the dopant species. At the doping level of $x = 1$ the octahedral sites are filled, and hence for $x = 2$ the remaining dopants were distributed evenly amongst the square pyramidal sites in order to maximise the separation between the dopant atoms (Fig. 2). In the second configuration, which we name "Square Pyramidal" the dopant species were distributed amongst alternating square pyramidal site at $x = 1$ and the square pyramidal sites were fully occupied when $x = 2$. For the final "Mixed" configuration the calculations were performed on a larger $(2(a + b), a - b, 2c)$ super-cell to allow for each of the two octahedral and the four square pyramidal layers to contain the same number of dopant atoms. For both $x = 1$ and $x = 2$ an equal number of dopant species were placed on each type of B-site, with the atoms distributed in order to maximise their separation (Fig. 2).

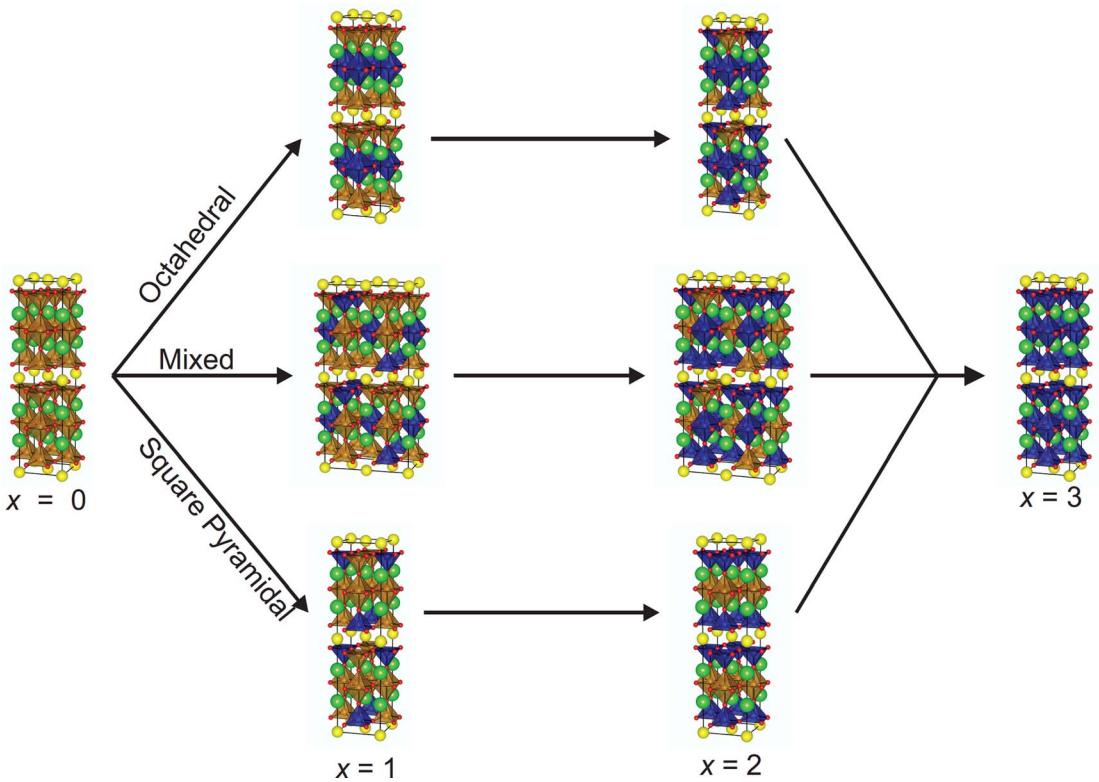

Fig. 2 Structures used for DFT calculations with the three different site preferences (octahedral, square pyramidal and mixed) at doping levels $x =$ 1 and 2. Atoms coloured as follows: Y (yellow), Ba (green), Fe (brown), dopant (blue) and oxygen (red).

Computational results

Balanced equations for the calculation of substitution energies were created taking into account the possibility of an overall change in oxygen content, depending on the dopant metal (ΔE_{sub}, Eqn (2)). Calculated values of ΔE_{sub} are used to predict whether a calculated composition would be stable (negative ΔE_{sub}) and therefore likely to form experimentally.

Results for the calculated substitution energies suggest that favourable doping can be achieved when M = Co and Mn and no favoured doping configuration was found when M = Ni. Substitution energies for the lowest energy configuration for each doping level and dopant are shown in Fig. 3a. When M = Co the $x = 1$ substitution level is favoured with $\Delta E_{sub} = -0.03$ eV/FU when the dopant atoms are distributed over octahedral and square-pyramidal sites in the Mixed configuration, *i.e.* with no B-site preference (Fig. 3b). At higher doping levels of $x = 2$ and 3, doping is calculated to be unfavourable, with positive values of ΔE_{sub}. The calculation of favourable doping for M = Co and $x = 1$ without any B-site preference which becomes unfavourable at a point between $x = 1$ and 2 is in good agreement with reported experimental results.[19] Co doping within the $YBa_2Fe_3O_8$ phase has been reported for the nominal values of $x = 0.6$, 0.9, 1.2 and 1.5, and substitution beyond $x = 1.5$ has not been reported

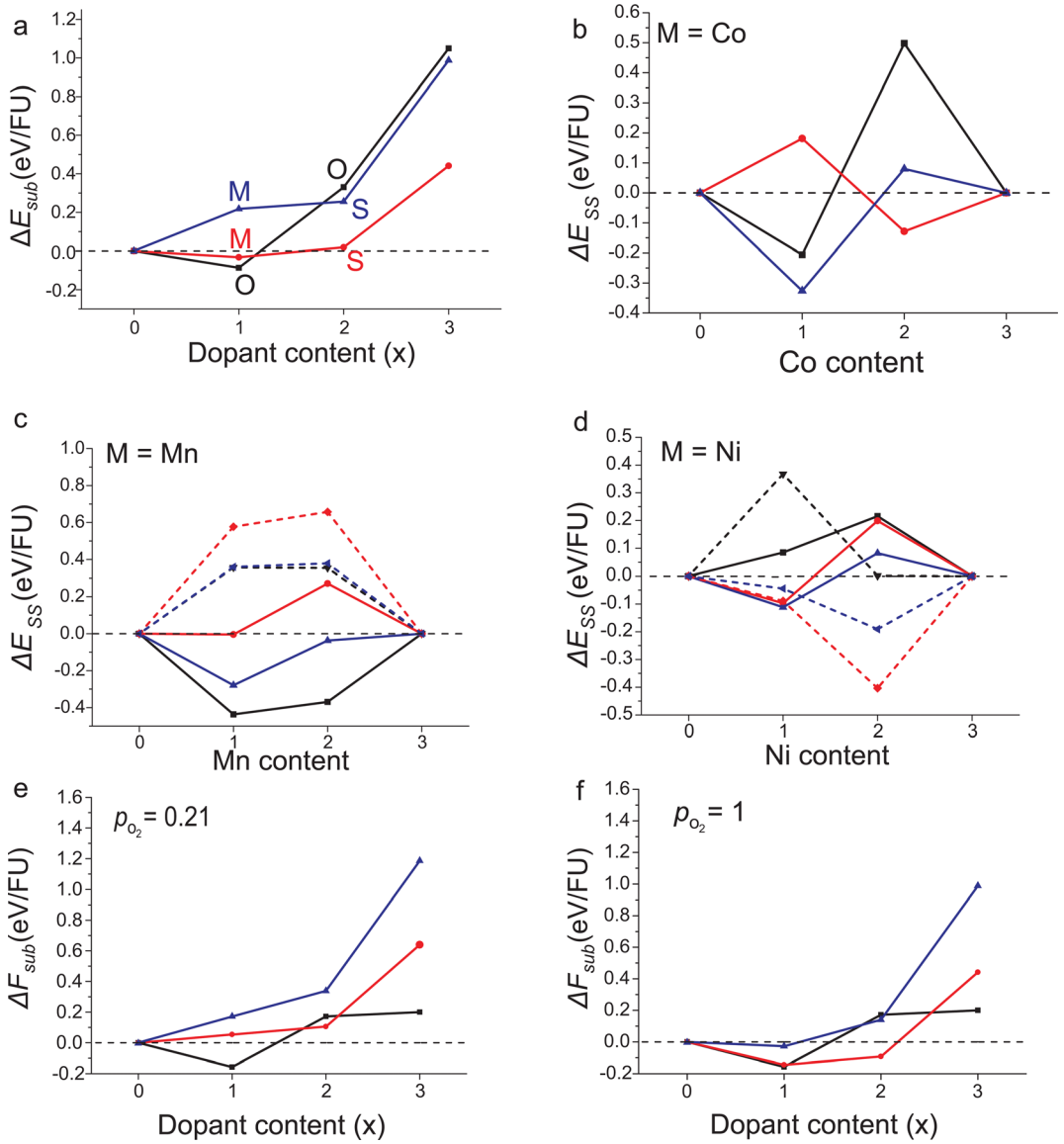

Fig. 3 (a) Calculated reaction energies, ΔE_{sub}, for the most stable configuration at each doping level for $YBa_2Fe_{3-x}M_xO_8$ calculated according to Eqn (2), for M = Mn (black), Co (red) and Ni (blue). The most stable configuration is indicated by the letters (octahedral), (mixed) and (square pyramidal). (b and c) Solid-solution energies, ΔE_{SS}, for all configurations and dopant species calculated according to Eqn (3). The octahedral (black), square pyramidal (red) and mixed (blue) configurations are plotted with solid lines for antiferromagnetic order and dashed lines for ferromagnetic order where calculated. $\Delta E_{SS} = 0$ in (c and d) to guide the eye. (e and f) Reaction free energies, ΔF_{sub}, calculated at 1473 K with partial oxygen pressures corresponding to air and pure O_2 at atmospheric pressure. Colours as in panel (a).

experimentally. In addition, experiments show no significant cation site preference for the doped compounds.[19] The consistency between the computational results and the experimentally reported phases suggest that our approach can reliably calculate the favourability of transition metal substitution within $YBa_2Fe_3O_8$.

For M = Mn calculations suggest that substitution is favoured at $x = 1$, with the Mn atoms in the octahedral configuration with G-type antiferromagnetic ordering on the B-site (Fig. 3c). ΔE_{sub} for the substituted material was calculated to be −0.09 eV/FU. The higher $x = 2$ substitution level is considerably unfavourable energetically; the most stable configuration has the Mn atoms in the octahedral configuration with G-type antiferromagnetic ordering but the substitution energy, ΔE_{sub}, is +0.33 eV/FU.

For M = Ni, no substitution level is found to have a negative value of ΔE_{sub}. An interesting result to note however, is that at $x = 2$ the Ni atoms were favoured in the square pyramidal sites and with ferromagnetic ordering (Fig. 3d). Although the $x = 2$ configuration was found to have a positive ΔE_{sub} value of +0.26 eV/FU, if this level of doping could be synthesised in the $3a_p$ structure, our calculations predict that the material would unusually favour ferromagnetic over G-type antiferromagnetic ordering.

In summary, the DFT calculations predict that only $x = 1$ Mn substitution is favourable from the six Ni and Mn substitution levels examined.

As expected, of the calculated structures we observe that for each doping level, the most stable configuration also has the smallest unit cell volume (Fig. 4a–c). The single exception was when $x = 1$ and M = Ni, where the configuration with the smallest unit cell volume is 0.014 eV/FU less stable compared to the structure with the lowest energy.

In the structure of the M = Mn, $x = 1$ octahedral configuration, which is predicted to be stable, the geometries (Fig. 4d) of the fully Mn occupied octahedral sites display a sharp increase in the distortion of the octahedral coordination environment when compared to the undoped material. The axial bond length increases by 0.11 Å with a concurrent shortening of the equatorial bond by 0.02 Å in line with the Jahn–Teller distortion expected for Mn^{3+} (Fig. 4d). When the doping level is increased ($x = 2$ and 3) the length of the equatorial bond changes little. However, the extra Mn atoms must be placed into square pyramidal sites, shortening one axial bond of the octahedron and creating an irregular octahedral site, with two long bonds (2.00 and 2.28 Å) and four short bonds with a mean length of 1.97 Å. Similarly at the doping level $x = 2$, where extra Mn atoms occupy half the square pyramidal sites, the square pyramid coordination environment distorts relative to the undoped material, resulting in four different square pyramids each with differing bond lengths. We suggest that the inclusion of Mn when x is greater than 1, forcing Mn into the square pyramidal sites and causing considerable distortion of all B-sites, is a factor which leads to the increased levels of doping becoming unfavourable.

The results presented above are based solely upon DFT ground state energies, however to predict the relative stability of phases under experimental conditions, it may be necessary to include the effects of finite temperature by calculating free energies of reaction. Free energies for the reaction shown in Eqn (2), ΔF_{sub}, have been calculated including contributions from the entropy of mixing and the free energy of gas phase O_2 (see ESI† for details).

Values of ΔF_{sub} calculated at the synthesis temperature of 1473 K, and with partial oxygen pressures corresponding to air

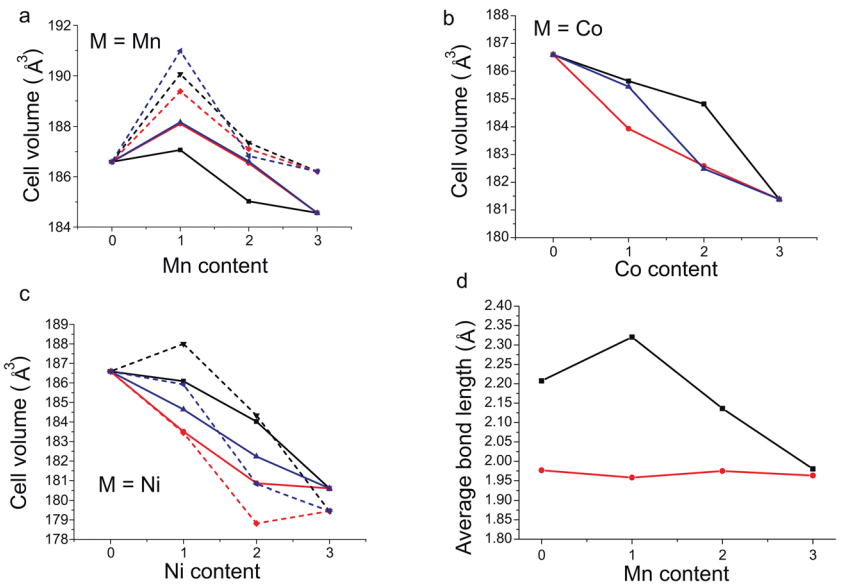

Fig. 4 (a–c) DFT unit cell volumes as a function of dopant content for Mn, Co and Ni. The octahedral (black), square pyramidal (red) and mixed (blue) configurations are plotted with solid lines for antiferromagnetic order and dashed lines for ferromagnetic order. (d) DFT calculated bond lengths for the axial (black) and equatorial (red) M–O bonds of the octahedral site as a function of Mn doping in the octahedral configuration of $YBa_2Fe_{3-x}Mn_xO_8$.

and pure O_2 at atmospheric pressure are shown in Fig. 3e and f. Qualitatively, the results follow closely those calculated at 0 K. All Ni doped compositions remain unstable at atmospheric partial oxygen pressure, although the data suggest that $YBa_2Fe_2NiO_8$ may be stable under an atmosphere of pure O_2, which is more oxidising than any conditions used experimentally in this study. Of the Mn doped compositions, $YBa_2Fe_2MnO_8$ retains a negative reaction energy and is predicted to be stable. The largest differences are seen in the Co doped compositions. Under air ($p_{O_2} = 0.21$) all Co doped compositions become unstable relative to $YBa_2Fe_3O_8$, Co_3O_4 and O_2; only under the more oxidising pure O_2 atmosphere ($p_{O_2} = 1$) is $YBa_2Fe_2CoO_8$ predicted to be stable. This is entirely in line with experiment, as synthesis of Co doped $YBa_2Fe_3O_8$ is carried out under flowing O_2.[19] In the present study, the conclusions drawn from pure DFT data, calculated at 0 K, would have been the same as those drawn from the free energy data. This may, however, not always be the case, and as our thermodynamic analysis required very little extra computational cost, we suggest that it should be carried out in any future studies which use a similar methodology.

Experimental results

To test both positive and negative predictions of doping levels, samples were synthesised at the composition $YBa_2Fe_2MnO_{8\pm\delta}$ (M = Mn, $x = 1$), which is predicted to be stable, and the compositions representing $YBa_2FeNi_2O_{8\pm\delta}$ (M = Ni, $x = 2$) and $YBa_2FeMn_2O_{8\pm\delta}$ (M = Mn, $x = 2$), predicted to be unstable. Synthesis was attempted in air and under a reducing atmosphere of flowing N_2.

In the sample with the composition $YBa_2FeNi_2O_{8\pm\delta}$ fired under flowing N_2 (Fig. 5a), it is observed that the sample contains a mixture of known binary and ternary oxide phases, with no formation of phases with the $3a_p$ structure. In the sample of composition $YBa_2FeMn_2O_{8\pm\delta}$ (Fig. 5b), the major phase was indexed to be a hexagonal perovskite similar to the reported 4H $BaMnO_{3-\delta}$,[33] along with two tetragonal or pseudotetragonal perovskite phases. One has lattice parameters of $a_p = 3.9270(2)$ Å and $c_p = 3.8380(4)$ Å, consistent with the double perovskite $YBaMn_2O_5$.[28] The other has perovksite lattice parameters of $a_p = 3.9004(9)$ Å and $c_p = 3.926(1)$ Å which are not consistent with any known phase containing these elements. No long range order peaks arising from a $3a_p$ phase were observed. The phases observed in $YBa_2FeNi_2O_{8\pm\delta}$ and $YBa_2FeMn_2O_{8\pm\delta}$ are in agreement with the predictions from DFT, in that a single $3a_p$ perovskite was not formed as the major phase in either sample.

In the $YBa_2FeNi_2O_{8\pm\delta}$ and $YBa_2Fe_2MnO_{8\pm\delta}$ samples that were fired under static air, no phases with the $3a_p$ structure were observed to form. With $YBa_2FeNi_2O_{8\pm\delta}$ the same impurity phases were observed as for flowing N_2, although with different relative intensities in the diffraction pattern, with intensities for the reported $YBa_3Fe_2O_{7.5}$ phase decreasing.[50] For the $YBa_2Fe_2MnO_{8\pm\delta}$ sample fired in static air, the two main phases were observed by XRD corresponding to $YFeO_3$ orthorhombic perovskite[51] and $BaMnO_3$ hexagonal perovskite (similar to that observed in the $YBa_2FeMn_2O_{8\pm\delta}$ sample described above).

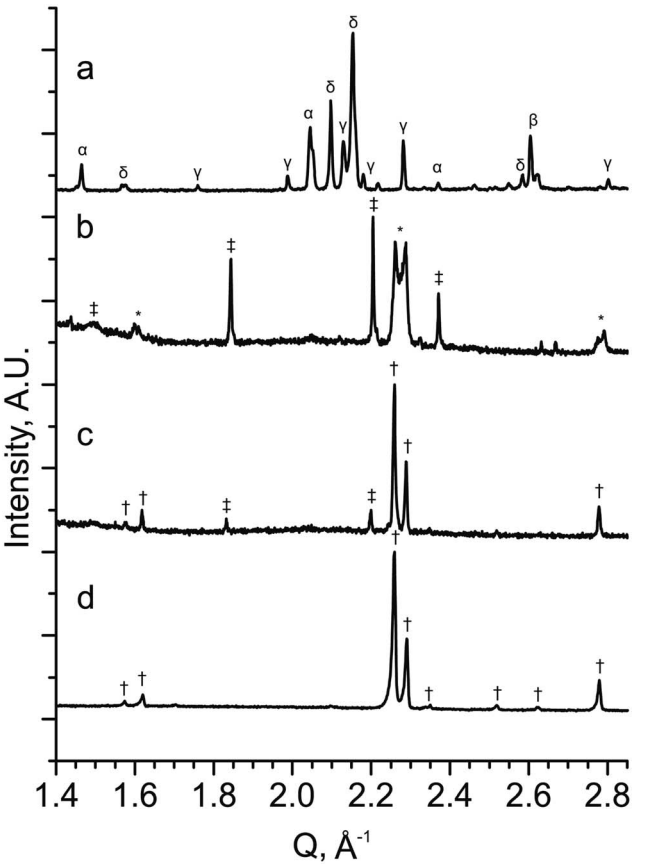

Fig. 5 PXRD patterns from stoichiometric samples of $YBa_2Fe_{3-x}M_xO_{8\pm\delta}$ for (a) M = Ni and $x = 2$ ($YBa_2FeNi_2O_{8\pm\delta}$), (b) M = Mn and $x = 2$ ($YBa_2FeMn_2O_{8\pm\delta}$) and (c) M = Mn and $x = 1$ ($YBa_2Fe_2MnO_{8\pm\delta}$) (d) $YBa_2Fe_2MnO_{8\pm\delta}$ with an optimised Y : Ba ratio ($Y_{1.175}Ba_{1.825}Fe_2MnO_{8\pm\delta}$) when synthesised under a N_2 atmosphere. The XRD patterns show that no $3a_p$ perovskite is formed in $YBa_2FeNi_2O_{8\pm\delta}$, with a mixture of oxide phase identified ($\alpha = Y_2O_3$, β = NiO, $\gamma = BaY_2NiO_5$ (ref. 63) and $\delta = YBa_3Fe_2O_{7.5}$ (ref. 50)). $YBa_2FeMn_2O_{8\pm\delta}$ contains a mix of hexagonal (‡) two cubic perovskite phases (*) with one of the perovskite phases similar to the $3a_p$ phase observed in pattern (d). $YBa_2Fe_2MnO_{8\pm\delta}$ contains a $3a_p$ perovskite (†) as the major phase with a minor hexagonal perovskite (‡) impurity identified as a $BaMnO_3$ type hexagonal perovskite. $Y_{1.175}Ba_{1.825}Fe_2MnO_{8\pm\delta}$ contains single phase $3a_p$ perovskite (†).

Diffraction data for $YBa_2Fe_2MnO_{8\pm\delta}$ fired under flowing N_2 (Fig. 5c) shows that the major phase is $3a_p$ perovskite, alongside a hexagonal impurity identified as similar to 10H $BaMn_{0.4}Fe_{0.6}O_{3-\delta}$.[52] The composition for $YBa_2Fe_2MnO_{8\pm\delta}$ was optimised to isolate the $3a_p$ component by altering the Y : Ba ratio. This was achieved by searching a one dimensional phase diagram covering $Y_yBa_{3-y}Fe_2MnO_8$ using 17 values ranging between 0.8 and 1.275 with varying intervals. The same synthetic procedure was maintained during this search under flowing N_2 gas, with a reduced target mass of 0.3 g. A phase pure material with the $3a_p$ structure was only obtained at the composition $Y_{1.175}Ba_{1.825}Fe_2MnO_{8\pm\delta}$ (Fig. 5d). Relatively minor decreases or increases of 0.025 in Y content resulted in impurities of 10H hexagonal perovskite or $YFeO_3$, respectively (Fig. 6a and c).

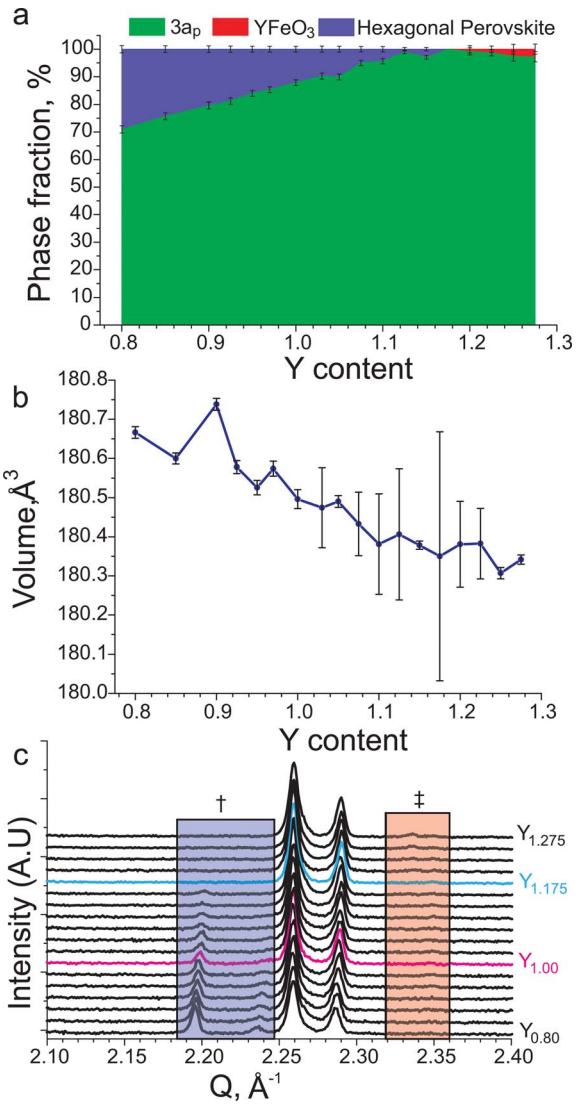

Fig. 6 (a) Refined phase fractions in $Y_yBa_{3-y}Fe_2MnO_{8\pm\delta}$ samples as a function of the Y content, $3a_p$ indicates the phase fraction of the desired phase, $YFeO_3$ indicates the phase fraction of a perovskite similar to the reported $YFeO_3$ material[51] and hexagonal perovskite similar to the reported 10H $BaMn_{0.4}Fe_{0.6}O_{3-\delta}$ material.[52] (b) Refined unit cell volumes for $Y_yBa_{3-y}Fe_2MnO_8$ samples as a function of the Y content. (c) Cu Kα_1 XRD patterns of $Y_yBa_{3-y}Fe_2MnO_{8\pm\delta}$ samples as a function of the Y content. The blue box labelled with † indicates the region where hexagonal perovskite reflections are observed and the red box marked with ‡ indicates the region where the main reflection for $YFeO_3$ perovskite is observed. The stoichiometric $YBa_2Fe_2MnO_{8\pm\delta}$ and phase-pure $Y_{1.175}Ba_{1.825}Fe_2MnO_{8\pm\delta}$ compositions have been plotted using red and blue lines respectively.

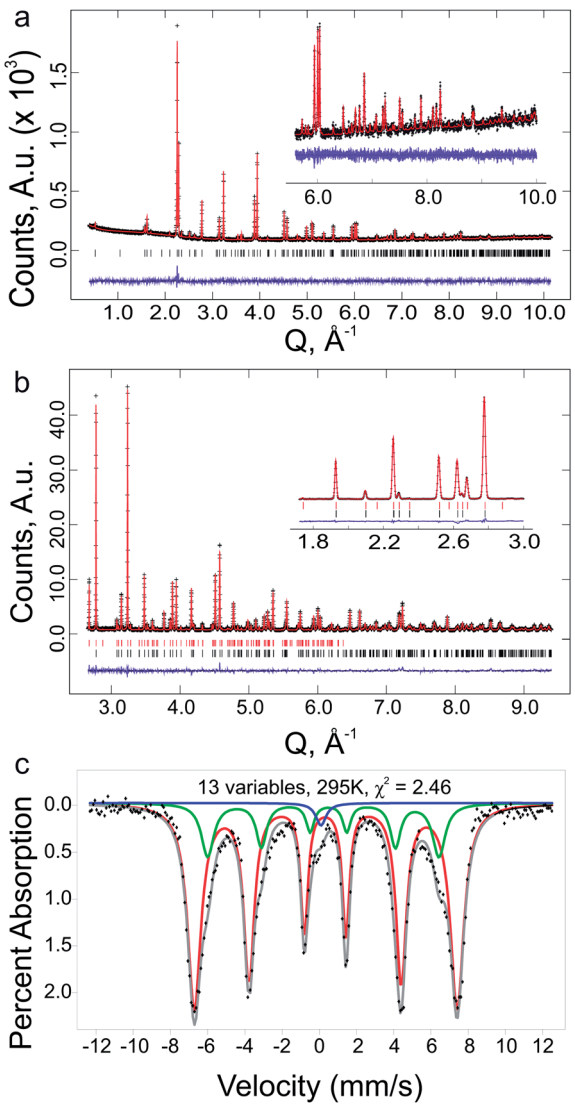

Fig. 7 (a) Rietveld plot for Mo Kα_1 PXRD data for phase pure $Y_{1.175}Ba_{1.825}Fe_2MnO_{8.04(5)}$, with high Q range in-set. (b) Rietveld plot for HRPD 168° bank containing both nuclear and magnetic phases for phase pure $Y_{1.175}Ba_{1.825}Fe_2MnO_{8.04(5)}$, with low Q range inset from HRPD 90° bank, black and red tick marks indicate the nuclear and magnetic *hkl* positions respectively. (c) Room temperature Mössbauer spectrum for phase pure $Y_{1.175}Ba_{1.825}Fe_2MnO_{8\pm\delta}$, showing a fit to two Fe^{3+} environments for the refined as octahedral and square pyramidal geometries, and a singlet at Fe signal at $\approx$ 0 mm s^{-1}, attributed to disordered Fe^{4+} in the system with an integrated area of 1.7(1) % of the total spectrum.

The oxygen content at the optimised composition, $Y_{1.175}Ba_{1.825}Fe_2MnO_{8\pm\delta}$, was analysed by iodometric titration. The determined oxygen content was $O_{8.04(5)}$, giving an average transition metal charge state of 2.97(3)+, assuming charge states of 3+ and 2+ on Y and Ba respectively. Mössbauer spectroscopy (Fig. 7c) of this sample shows the material to be magnetically ordered at room temperature. The spectrum showed the presence of two Fe^{3+} sites, which were refined as consistent with octahedral and square pyramidal geometries. In addition a small paramagnetic Fe^{4+} signal was observed, and modelled as disordered over both sites. The distribution of Fe atoms within the structure was refined as 80(1) % in square pyramidal geometry and 20(1) % in octahedral geometry. Using the assumption that the only other species on the same sites is Mn, and that there is a fixed ratio between square pyramidal and octahedral sites of 2 : 1, the distribution of Mn atoms is 40(1) % square pyramidal and 60(1)% octahedral.

Refinement of the $3a_p$ unit cell as a function of the Y content over the $Y_yBa_{3-y}Fe_3O_8$ range, shows that there is a small variation in the unit cell volume (Fig. 6b). The variation in the cell

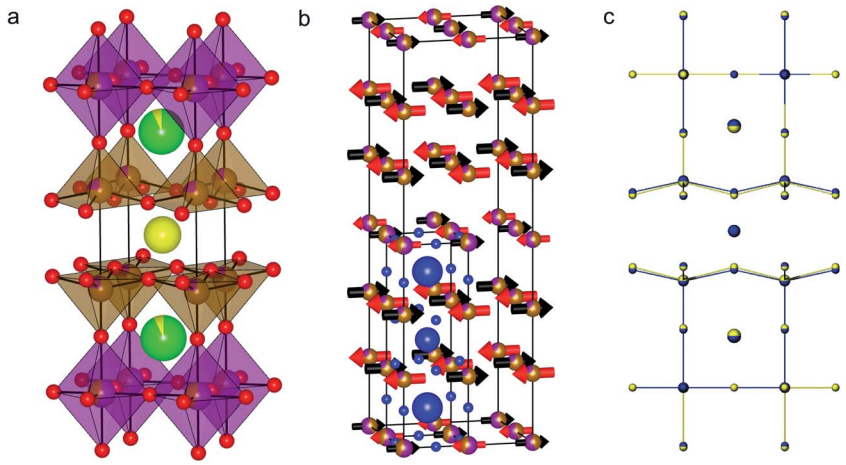

Fig. 8 (a) The refined nuclear structure of $Y_{1.175}Ba_{1.825}Fe_2MnO_{8.04(5)}$ and (b) the refined magnetic structure. For clarity the atoms from the nuclear unit cell are overlaid in blue. (c) The observed $Y_{1.175}Ba_{1.825}Fe_2MnO_{8.04(5)}$ structure (blue) overlaid with the DFT predicted cell (yellow). Note that the unit cell sizes have been normalised to the observed cell for clarity in observing the similarity between the observed and predicted atomic coordinates.

volume implies that the structure should be accessible over a range of compositions; however, in our studies we only access the structure phase pure at one specific composition. This suggests that variation of the Fe : Mn ratio is also required at each Y : Ba ratio in order to synthesise the phase pure structure over a range of compositions, this was not attempted within this work as the Fe : Mn ratio was the focus of the DFT investigation, and the appropriate Y : Ba ratio was determined for the Fe : Mn ratio studied.

The results of DFT calculations were used as the basis for the structural refinement of $Y_{1.175}Ba_{1.825}Fe_2MnO_{8.04(5)}$. The symmetry of the calculated $YBa_2Fe_2MnO_8$ structure with octahedrally coordinated Mn atoms was determined using the FINDSYM code[53] (version 3.2.3, with the tolerance set to 0.1 Å). The highest symmetry space group was determined to be tetragonal *P4/mmm* (Fig. 8a) in a unit cell where $a = b = 3.91603$ and $c = 12.19815$ Å. In order to be consistent with reported structures for the undoped material the origin of the unit cell was set to be at the octahedral B-site. The observed B-site occupancies from Mössbauer spectroscopy were used as the starting model for B-site ordering within the structure.

For the Rietveld refinement of $Y_{1.175}Ba_{1.825}Fe_2MnO_{8.04(5)}$, the structure was entered into GSAS[64,65] as separate nuclear (PXRD and NPD) and magnetic (NPD only) phases. Following earlier refinements of the magnetic structure of $YBa_2Fe_3O_8$,[54] the magnetic cell was refined as a ($2a$, $2b$, $2c$) super-cell of the orthorhombic nuclear cell, in the orthorhombic $Fmm'm'$ magnetic space group configured in a G-type antiferromagnetic structure (see ESI† for further details). Constraints were setup between the two phases in order to keep the B-site atoms consistent (positions, occupancies and thermal parameters were constrained) and the unit cells and phase fractions of the two phases were fixed, so that the ratio of the lattice parameters and total number of B-site atoms was maintained between the nuclear and magnetic phases.

As the starting model for the structure refinement of $Y_{1.175}Ba_{1.825}Fe_2MnO_{8.04(5)}$ was the atomic structure from the DFT model as described above, the composition was initially set close to the nominal value at $Y_{1.16}Ba_{1.84}Fe_2MnO_8$, with the additional Y inserted onto the Ba A-site. As the Rietveld refinement progressed, the composition was allowed to refine with the only restraint being that full occupancy was enforced at each metal site. During the Rietveld refinement the space group was changed to *Pmmm* to allow an orthorhombic distortion in the lattice parameters to improve the fit of broader reflections with *hkl* values where $h \neq k$. The refined orthorhombic distortion is small with a strain $(a - b)/(a + b)$ of 0.04%, and is presumably related to spin–orbit coupling which is not included in the current DFT calculations. The final Rietveld plots can be found in Fig. 7a and b, the resulting structure is shown in Fig. 8b and the results of the refinements are given in Tables 1 and 2, the reduced χ^2 was 4.46 for 72 variables.

Refinement of the oxygen content was trialled during the structure analysis. No vacancies were observed on the five oxygen positions and no extra oxygen within the structure could be found. This was trialled by placing an extra oxygen site in plane with the Y site (A1 in Table 1), previously reported as the O4 site in the undoped material.[18] As no additional oxygen or any oxygen vacancies were found, the oxygen content was fixed to the nominal value of O_8 in the final refinement, which is in good agreement with the oxygen content observed from iodometry ($O_{8.04(5)}$).

During Rietveld refinement, the A-site ratios in $Y_{1.175}Ba_{1.825}Fe_2MnO_{8.04(5)}$ changed from the starting values with small changes to the B-site ratio, to give a refined composition of $Y_{1.14(1)}Ba_{1.86(1)}Fe_{1.961(4)}Mn_{1.039(4)}O_8$, a result close to the nominal composition of $Y_{1.175}Ba_{1.825}Fe_2MnO_{8.04(5)}$. The composition of $Y_{1.175}Ba_{1.825}Fe_2MnO_{8.04(5)}$ contains an excess of Y that occupies the A2 site together with Ba (Table 1). When trialled in the refinement there was no observed disorder on the A1 site which remained fully occupied by Y. The atomic coordinates of the refined structure show little deviation from those of the DFT structure (Fig. 8c and Table 1), with the exception of a small orthorhombic distortion and the z positions of O1 and O2 (Table 1). O1 and O2 are no longer related by symmetry due to the

Table 1 Refined crystallographic data and DFT structure parameters for $Y_{1.175}Ba_{1.825}Fe_2MnO_{8.04(5)}$ refined in *Pmmm* space group. Note that all sites were constrained to be fully occupied. Refined parameters shown in bold[a]

Parameter	Rietveld	DFT
a (Å)	**3.88407(5)**	3.91603
b (Å)	**3.88125(5)**	3.91603
c (Å)	**11.98425(9)**	12.19815

Rietveld (*Pmmm*)					DFT (*P*4/*mmm*)		
Site	Position	Composition	U_{iso} (Å^2)	Multiplicity	Position	Composition	Multiplicity
A1	0.5, 0.5, 0.5	Y	**0.0127(2)**	1	0.5, 0.5, 0.5	Y	1
A2	0.5, 0.5, **0.83558(7)**	**$Ba_{0.929(5)}Y_{0.071(5)}$**	**0.0127(2)**	2	0.5, 0.5, 0.833890	Ba	2
B1	0, 0, **0.66045(6)**	**$Fe_{0.762(1)}Mn_{0.238(1)}$**	**0.013(1)**	2	0, 0, 0.656840	Fe	2
B2	0, 0, 0	**$Fe_{0.437(2)}Mn_{0.563(2)}$**	**0.0091(2)**	1	0, 0, 0	Mn	1
O1	0.5, 0, **0.3757(1)**	O	**0.0133(5)**	2	0, 0.5, 0.385130	O	4
O2	0, 0.5, **0.3880(1)**	O	**0.0175(6)**	2	Equivalent to O1		
O3	0, 0, **0.81499(8)**	O	**U_{11} 0.035(2) U_{22} 0.024(1) U_{33} 0.0224(6)**	2	0, 0, 0.809780	O	2
O4	0.5, 0, 0	O	**0.0067(6)**	1	0.5, 0, 0	O	2
O5	0, 0.5, 0	O	**0.0135(7)**	1	Equivalent to O4		

[a] Total refined composition: $Y_{1.14(1)}Ba_{1.86(1)}Fe_{1.961(4)}Mn_{1.039(1)}O_8$, formula weight = 651.37 g mol^{-1}, formula units per cell = 1.

Table 2 Refined crystallographic data for the magnetic structure of $Y_{1.175}Ba_{1.825}Fe_2MnO_{8.04(5)}$ and relationships to structure parameters in Table 1. Note all parameters apart from the magnetic moments are linked with equivalent parameters in the nuclear structure. The refined magnetic cell contains 8 formula units

	Parameter	Rietveld	Relationship to nuclear
	a (Å)	7.76814(9)	$\times 2\ a_{nuclear}$
	b (Å)	7.76248(9)	$\times 2\ b_{nuclear}$
	c (Å)	23.9684(2)	$\times 2\ c_{nuclear}$
Site	Parameter	Rietveld	Equivalent nuclear site (Table 1)
1a	Position	0, 0, 0	B2
	Composition	$Fe_{0.437(2)}Mn_{0.563(2)}$	
	U_{iso} (Å^2)	0.0091(2)	
	μ_B	−2.81(4)	
	Multiplicity	4	
1b	Position	0, 0, 0.5	B2
	Composition	$Fe_{0.437(2)}Mn_{0.563(2)}$	
	U_{iso} (Å^2)	0.0091(2)	
	μ_B	+2.81(4)	
	Multiplicity	4	
2a	Position	0, 0, 0.33025(3)	B1 $z = z_{nuclear}/2$
	Composition	$Fe_{0.762(1)}Mn_{0.238(1)}$	
	U_{iso} (Å^2)	0.013(1)	
	μ_B	−3.41(3)	
	Multiplicity	8	
2b	Position	0, 0, 0.16975(3)	B1 $z = ½ - z_{nuclear}/2$
	Composition	$Fe_{0.762(1)}Mn_{0.238(1)}$	
	U_{iso} (Å^2)	0.013(1)	
	μ_B	+3.41(3)	
	Multiplicity	8	

orthorhombic distortion away from the calculated tetragonal *P*4/*mmm* structure, and have different heights in the cell such that the basal planes of the square pyramids are slightly buckled.

Ordering between the two B-site geometries in the refined structure was observed to change little from the starting values of $Fe_{0.8}Mn_{0.2}$ (B1) and $Fe_{0.4}Mn_{0.6}$ (B2) for the square pyramidal and octahedral sites respectively, which were set to the refined Mössbauer occupancies. The refined site occupancies were $Fe_{0.762(1)}Mn_{0.238(1)}$ for the square pyramidal site and $Fe_{0.437(2)}Mn_{0.563(2)}$ for the octahedral site, a 4% difference from values refined using room temperature Mössbauer spectroscopy (Fig. 7c). Note that due to the large contrast in neutron scattering between Fe and Mn (coherent scattering lengths of 9.45 fm and −3.73 fm, respectively[55]), the refinement of the occupation of this site is reliable. The magnetic moments for the B-sites were refined to be 3.41(3) and 2.81(4) μ_B for the square pyramidal and octahedral sites respectively, consistent with the square pyramidal site hosting more Fe relative to the octahedral site.

Discussion

The initial DFT screening of potential doping onto the Fe site of $YBa_2Fe_3O_8$ was successful in predicting a favourable doping species (Mn) and content ($YBa_2Fe_2MnO_8$), which was previously unreported in the $3a_p$ structure. We note, however, that considerable experimental work was still required to obtain a pure doped compound and characterize it, with slight differences in stoichiometry and structure compared to that predicted computationally.

To reduce computational expense, DFT calculations were limited to stoichiometric compositions in which the average oxidation state on the B-site was restricted to 3+, or equivalently, the oxygen content was fixed to 8. Experimentally however, the sample composition and atmosphere used during synthesis

were tuned to control the average transition metal charge state to near 3+ and to stabilise the $3a_p$ phase relative to other competing phases containing Mn in a 4+ state. Successful experimental synthesis of pure $3a_p$ $Y_{1.175}Ba_{1.825}Fe_2MnO_{8.04(5)}$ required alteration of the A-site charge away from stoichiometry and control of oxygen partial pressure during synthesis using N_2 gas, as synthesis in air and synthesis with lower average A-site charge state both resulted in the formation of Mn^{4+} containing species in preference to $3a_p$. In this case performing a calculation at the exact composition was not necessary to predict the initial doping success, however experimental refinement of the composition was still required to isolate the compound. Comparing the structure of the DFT predicted compound, $YBa_2Fe_2MnO_8$, with the Rietveld refined structure of $Y_{1.175}Ba_{1.825}Fe_2MnO_{8.04(5)}$, we find that the calculated unit cell volume is within 3.5% of experiment, with a similar agreement between the reported and calculated cell volumes for the undoped material.

One could envision calculating reaction energies for a number of non-stoichiometric compositions. However, for each composition larger super-cells and more configurations would be required in order to determine the most stable cation arrangement. Additional complexity is introduced by the necessity of modelling the inevitably disordered A-sites, as well as potentially disordered B-sites. Hence we suggest that a computational investigation of small changes in stoichiometry is unfeasible at present.

To quantify the level of ordering between Fe and Mn on the B-sites, we define the parameter $\Phi = (3f - 1)/2$, where f is the fraction of Mn on the octahedral sites. DFT calculations predicted a complete segregation of Mn to the octahedral sites in $YBa_2Fe_2MnO_8$ ($\Phi = 1$), in a completely disordered system 1/3 of the octahedral sites would be occupied by Mn ($\Phi = 0$), and experimentally the fraction of octahedral sites occupied by Mn was refined to 0.563(2) ($\Phi = 0.34$). To model the expected extent of ordering at finite temperatures based on 0 K DFT energies, a statistical mechanics approach described in the ESI,†[30] was applied to the six configurations used for the DFT calculations at the composition $YBa_2Fe_2MnO_8$. When the occupations of the B-sites are estimated at the synthesis temperature of 1475 K, there is a preference for Mn in the octahedral site, though substantial mixing of Fe and Mn is predicted, with $\Phi = 0.57$. At 300 K, however, the structure is predicted to be very close to fully ordered with $\Phi = 0.996$. Under cooling during synthesis, cation motion will be frozen out at high temperatures, trapping the structure in a state with some site disorder due to configurational entropy. This explains the deviation of the refined value of $\Phi = 0.34$ away from fully ordered $\Phi = 1$, but shows that the 0 K DFT calculations had calculated the correct site preference for Mn within the structure.

A small, but significant difference between the calculated and experimental structure is the slight orthorhombic distortion of the refined nuclear structure. The tetragonal parent material, $YBa_2Fe_3O_8$, is reported to become orthorhombic upon introduction of oxygen vacancies to form $YBa_2Fe_3O_{8-\delta}$ ($\delta \geq 0.14$).[21] It is possible that the orthorhombic distortion observed in $Y_{1.175}Ba_{1.825}Fe_2MnO_{8.04(5)}$ is similarly due to oxygen vacancies, however we note that this is not supported by the results of iodometric titration or attempts to refine oxygen contents away from stoichiometry. An alternative explanation is that spin–orbit coupling of the antiferromagnetically ordered electronic spins, which necessarily have orthorhombic symmetry, has caused an orthorhombic distortion of the nuclear structure as reported for the mixed valence compound $YBaFe_2O_5$.[56] In both cases, the orthorhombic distortion is accompanied by buckling of the basal planes of the square pyramidal sites, as observed here for $Y_{1.175}Ba_{1.825}Fe_2MnO_{8.04(5)}$. Neither effect would be captured in the stoichiometric DFT calculations performed with collinear spin and neglecting spin–orbit interactions. The present experimental data are unable to distinguish between the two potential causes of this orthorhombic distortion.

The refined structure of $Y_{1.175}Ba_{1.825}Fe_2MnO_{8.04(5)}$ shows that the unit cell distorts upon doping compared to $YBa_2Fe_3O_8$ (ref. 18) by a 0.9% shortening of the a and b axes and a concurrent 1.4% lengthening of the c axis. This results in a 2.3% increase in the average c/a ratio upon doping, and a 0.5% reduction in cell volume. These changes in cell shape can be related to changes in the M–O bonding environments upon doping, seen in the comparison of the M–O bonds of $Y_{1.175}Ba_{1.825}Fe_2MnO_{8.04(5)}$ and $YBa_2Fe_3O_8$ (Table 3). As observed in the DFT calculations, experimentally the M_{Oct} – O_{Axial} bond on the octahedral site is seen to lengthen on doping by 4.2% (0.094(3) Å), consistent with the expected Jahn–Teller distortion when accommodating Mn^{3+} in an octahedral site. The elongation of the unit cell upon doping is largely due to this Jahn–Teller distortion.

We used the methodology reported by Baur[57] implemented in VESTA[58] to further quantify the distortions of the polyhedra in the $3a_p$ structure by calculation of a distortion parameter according to the following equation:

$$D = \frac{1}{n}\sum_{i=1}^{n}\left(\frac{|L_i - L_{avg}|}{L_{avg}}\right) \quad (4)$$

where D is the distortion parameter, n is the number of bonds in the polyhedron, L_i is the length of bond i, and L_{avg} is the average bond length in the polyhedron. An undistorted polyhedron

Table 3 Observed and calculated bond lengths for $YBa_2Fe_3O_8$ ($x = 0$) and $Y_{1.175}Ba_{1.825}Fe_2MnO_{8.04(5)}$ ($x = 1$)

Bond	$YBa_2Fe_3O_8$ observed[18] (Å)	$Y_{1.175}Ba_{1.825}Fe_2MnO_{8.04(5)}$ observed (Å)	$YBa_2Fe_3O_8$ DFT (Å)	$YBa_2Fe_2MnO_8$ DFT (Å)
M_{oct} – $O_{equatorial}$	1.9590	1.94204(3) – O4, 1.94062(3) – O5, **1.94133(3) average**	1.9767	1.9580
M_{oct} – O_{axial}	2.1807(17)	2.2173(10) – O3	2.2074	2.3203
$M_{sq.py}$ – $O_{equatorial}$	2.0198(4)	1.9894(4) – O1, 2.0259(5) – O2, **2.0077(5) average**	2.0407	2.0240
$M_{sq.py}$ – O_{axial}	1.8405(24)	1.8513(12) – O3	1.8597	1.8649

Table 4 Distortion parameters calculated in VESTA according to Eqn (4).[57] Note that the values quoted for the distortion parameters for the $YBa_2Fe_2MnO_8$ the values given in italics indicate average values for Fe and Mn atoms as both Fe and Mn atoms are found in the same co-ordination environment in the configuration, configurations highlighted in bold for DFT configurations indicate the lowest energy configuration

Geometry	$YBa_2Fe_3O_8$ observed (literature)[18]	$Y_{1.175}Ba_{1.825}Fe_2MnO_{8.04(5)}$ observed (this work)	$YBa_2Fe_3O_8$ DFT	$YBa_2Fe_2MnO_8$ DFT
Square pyramid	0.0226	0.0254	**0.0289**	**0.026 (Octahedral configuration)** *0.020 (Square Pyramidal configuration)* *0.027 (Mixed configuration)*
Octahedral	0.0385	0.0603	**0.0491**	**0.078 (Octahedral configuration)** *0.060 (Square Pyramidal configuration)* *0.074 (Mixed configuration)*

would yield a value of zero and an example of heavily distorted octahedra is found in the $Bi_4Ti_3O_{12}$ structure which gives values of 0.078 and 0.119.[59] Values for the experimental structures of $Y_{1.175}Ba_{1.825}Fe_2MnO_{8.04(5)}$ and $YBa_2Fe_3O_8$ are shown in Table 4. The octahedral site is observed to distort significantly upon doping, with the distortion parameter changing from 0.039 to 0.060 (an increase of 56.6%), driven by the aforementioned elongation of the axial bond. The square pyramidal site sees a much smaller shift in its distortion parameter, changing from 0.023 to 0.025 (an increase of 12.4%), although a split in equatorial bond lengths from a single bond length of 2.0198(4) Å in $YBa_2Fe_3O_8$ (ref. 18) to 1.9894(4) Å and 2.0259(5) Å in $Y_{1.175}Ba_{1.825}Fe_2MnO_{8.04(5)}$ is observed (Table 3), giving rise to a buckling in the basal planes of the square pyramidal sites. It is interesting to note that the undoped compound, $YBa_2Fe_3O_8$, contains octahedral sites which are already distorted, with two long bonds and four short bonds, even though no Jahn–Teller distortion would be expected for high spin d^5 Fe^{3+}. It is possible that this distortion already evident within the $3a_p$ structure leads to the octahedral site being particularly favourable for hosting Jahn–Teller active Mn^{3+} ions, and similar sites in other Fe^{3+} oxides could be targeted for doping with Mn^{3+}.

Although this is the first reported mixed Fe/Mn compound with the $3a_p$ structure, other perovskite based Fe/Mn oxides have been reported, and show similar site preferences. For example, the brownmillerite $Ca_2Fe_2O_5$ has similarly distorted octahedral sites, with $D = 0.045$.[24] Introduction of Mn into the compound to form $Ca_2Fe_{1.039(8)}Mn_{0.962(8)}O_5$ (ref. 27) leads to an increase in the distortion of the octahedral sites ($D = 0.066$), with Mn preferred in these sites. There are, however, many other examples of Mn^{3+} doping into perovskite based structures, in which the Mn^{3+} is coordinated in octahedral geometry,[27,60] square pyramidal geometry[28] or with B-site disorder.[61,62] By the use of DFT we have been able to clearly predict the correct B-site ordering within a $3a_p$ structure, even though precedents exist for all possible alternatives in known structures.

Conclusions

In summary, we have shown that it is possible to use DFT calculations to obtain reaction enthalpies to form complex oxides from binary oxides; we have then been able to use this method to predict a stable doping level in the $YBa_2Fe_3O_8$ structure, with the Mn doping level of $x = 1$ and Mn atoms preferentially doping onto the already distorted octahedral site and increasing the level of distortion. We also have rationalised why doping becomes unfavourable when $x = 2$ and M = Mn; increasing the doping level above 1 forces a larger proportion of Mn atoms into the square pyramidal sites which in turn results in a less distorted octahedral geometry. These calculations have been able to successfully predict the approximate composition, B-site ordering (and distortion of B-sites, Fig. 8c) and accurate atomic coordinates of the doped structure of an oxide where the ordering is between two similar transition metals. The predicted material was then synthesised with only small deviations in the structure and composition.

We have shown that using this methodology, we were able to predict compositions for which the formation of the $3a_p$ structure is favourable or unfavourable, and that these results match subsequent experimental observations. We therefore conclude that the methodology presented here can be used as a powerful tool to guide the synthesis of new materials by chemical substitution and can be used for large and or complex oxides where the systems are too large or complex for existing methods.

Acknowledgements

This work was funded by the European Research Council (ERC Grant Agreement 227987 RLUCIM). We thank EPSRC for a studentship to C. Collins. We gratefully acknowledge ISIS and the STFC Rutherford Appleton Laboratory for provision of neutron diffraction facilities and Aziz Daoud-Aladine for assistance in using HRPD. Structural images were made using VESTA.[58] MJR thanks the Royal Society for the award of a Research Professorship.

References

1 M. A. Pena and J. L. G. Fierro, *Chem. Rev.*, 2001, **101**, 1981–2017.
2 A. Aguadero, L. Fawcett, S. Taub, R. Woolley, K. T. Wu, N. Xu, J. A. Kilner and S. J. Skinner, *J. Mater. Sci.*, 2012, **47**, 3925–3948.
3 T. Minami, *Semicond. Sci. Technol.*, 2005, **20**, S35–S44.
4 J. P. Attfield, *J. Mater. Chem.*, 2011, **21**, 4756–4764.

5 V. V. Shvartsman and D. C. Lupascu, *J. Am. Ceram. Soc.*, 2012, **95**, 1–26.
6 L. B. Kong, S. Li, T. S. Zhang, J. W. Zhai, F. Y. C. Boey and J. Ma, *Prog. Mater. Sci.*, 2010, **55**, 840–893.
7 J. W. Fergus, *J. Eur. Ceram. Soc.*, 2012, **32**, 525–540.
8 Y. L. Chen and S. F. Yang, *Adv. Appl. Ceram.*, 2011, **110**, 257–269.
9 R. C. Pullar, *Prog. Mater. Sci.*, 2012, **57**, 1191–1334.
10 J.-I. Jung, S. T. Misture and D. D. Edwards, *Solid State Ionics*, 2010, **181**, 1287–1293.
11 J. Pena-Martinez, D. Marrero-Lopez, J. C. Ruiz-Morales, P. Nunez, C. Sanchez-Bautista, A. J. Dos Santos-Garcia and J. Canales-Vazquez, *Int. J. Hydrogen Energy*, 2009, **34**, 9486–9495.
12 Z. P. Shao and S. M. Haile, *Nature*, 2004, **431**, 170–173.
13 A. Yan, M. Yang, Z. Hou, Y. Dong and M. Cheng, *J. Power Sources*, 2008, **185**, 76–84.
14 P. K. Nayak, J. Yang, J. Kim, S. Chung, J. Jeong, C. Lee and Y. Hong, *J. Phys. D: Appl. Phys.*, 2009, **42**, 035102.
15 H. Agura, A. Suzuki, T. Matsushita, T. Aoki and M. Okuda, *Thin Solid Films*, 2003, **445**, 263–267.
16 R. E. Treharne, K. Hutchings, D. A. Lamb, S. J. C. Irvine, D. Lane and K. Durose, *J. Phys. D: Appl. Phys.*, 2012, **45**, 335102.
17 R. J. Cava, A. W. Hewat, E. A. Hewat, B. Batlogg, M. Marezio, K. M. Rabe, J. J. Krajewski, W. F. Peck Jr and L. W. Rupp Jr, *Physica C*, 1990, **165**, 419–433.
18 P. Karen, E. Suard and F. Fauth, *Inorg. Chem.*, 2005, **44**, 8170–8172.
19 Q. Z. Huang, V. L. Karen, A. Santoro, A. Kjekshus, J. Lindén, T. Pietari and P. Karen, *J. Solid State Chem.*, 2003, **172**, 73–80.
20 P. Karen and A. Kjekshus, *J. Solid State Chem.*, 1994, **112**, 73–77.
21 P. Karen, A. Kjekshus, Q. Huang, V. L. Karen, J. W. Lynn, N. Rosov, I. Natali Sora and A. Santoro, *J. Solid State Chem.*, 2003, **174**, 87–95.
22 I. Felner, I. Nowik, U. Yaron, O. Cohen, E. R. Bauminger, T. Kroener and G. Czjzek, *Phys. Rev. B: Condens. Matter Mater. Phys.*, 1993, **48**, 16040–16046.
23 Q. Huang, P. Karen, V. L. Karen, A. Kjekshus, J. W. Lynn, A. D. Mighell, N. Rosov and A. Santoro, *Phys. Rev. B: Condens. Matter Mater. Phys.*, 1992, **45**, 9611–9619.
24 A. L. Shaula, Y. V. Pivak, J. C. Waerenborgh, P. Gaczyñski, A. A. Yaremchenko and V. V. Kharton, *Solid State Ionics*, 2006, **177**, 2923–2930.
25 A. Demont, M. S. Dyer, R. Sayers, M. F. Thomas, M. Tsiamtsouri, H. N. Niu, G. R. Darling, A. Daoud-Aladine, J. B. Claridge and M. J. Rosseinsky, *Chem. Mater.*, 2010, **22**, 6598–6615.
26 F. Ramezanipour, J. E. Greedan, L. M. D. Cranswick, V. O. Garlea, R. L. Donaberger and J. Siewenie, *J. Am. Chem. Soc.*, 2012, **134**, 3215–3227.
27 F. Ramezanipour, B. Cowie, S. Derakhshan, J. E. Greedan and L. M. D. Cranswick, *J. Solid State Chem.*, 2009, **182**, 153–159.
28 F. Millange, E. Suard, V. Caignaert and B. Raveau, *Mater. Res. Bull.*, 1999, **34**, 1–9.
29 G. Hautier, C. Fischer, V. Ehrlacher, A. Jain and G. Ceder, *Inorg. Chem.*, 2011, **50**, 656–663.
30 R. Grau-Crespo, S. Hamad, C. R. A. Catlow and N. H. de Leeuw, *J. Phys.: Condens. Matter*, 2007, **19**, 256201.
31 B. J. Morgan and G. W. Watson, *J. Phys. Chem. Lett.*, 2011, **2**, 1657–1661.
32 S. Benny, R. Grau-Crespo and N. H. de Leeuw, *Phys. Chem. Chem. Phys.*, 2009, **11**, 808–815.
33 J. J. Adkin and M. A. Hayward, *J. Solid State Chem.*, 2006, **179**, 70–76.
34 Q. Wang, R. Grau-Crespo and N. H. de Leeuw, *J. Phys. Chem. B*, 2011, **115**, 13854–13861.
35 Q. Wang and N. H. de Leeuw, *Mineral. Mag.*, 2008, **72**, 525–529.
36 Y. Seminovski, P. Palacios, P. Wahnon and R. Grau-Crespo, *Appl. Phys. Lett.*, 2012, **100**, 102112.
37 D. O. Scanlon and A. Walsh, *Appl. Phys. Lett.*, 2012, **100**, 251911.
38 B. Saha, J. Acharya, T. D. Sands and U. V. Waghmare, *J. Appl. Phys.*, 2010, **107**, 033715.
39 D. J. Fredeman, P. H. Tobash, M. A. Torrez, J. D. Thompson, E. D. Bauer, F. Ronning, W. W. Tipton, S. P. Rudin and R. G. Hennig, *Phys. Rev. B: Condens. Matter Mater. Phys.*, 2011, **83**, 224102.
40 M. Pishahang, C. E. Mohn, S. Stolen and E. Bakken, *RSC Adv.*, 2012, **2**, 10667–10672.
41 Y. L. Lee, J. Kleis, J. Rossmeisl and D. Morgan, *Phys. Rev. B: Condens. Matter Mater. Phys.*, 2009, **80**, 224101.
42 M. Regulski, R. Przeniosło, I. Sosnowska, D. Hohlwein and R. Schneider, *J. Alloys Compd.*, 2004, **362**, 236–240.
43 D. Rodic, V. Spasojevic, V. Kusigerski, R. Tellgren and H. Rundlof, *Phys. Status Solidi B*, 2000, **218**, 527–536.
44 M. Catti, G. Valerio and R. Dovesi, *Phys. Rev. B: Condens. Matter Mater. Phys.*, 1995, **51**, 7441–7450.
45 M. Faucher and J. Pannetier, *Acta Crystallogr., Sect. B: Struct. Sci.*, 1980, **36**, 3209–3211.
46 L. G. Liu, *J. Appl. Phys.*, 1971, **42**, 3702–3704.
47 W. L. Roth, *J. Phys. Chem. Solids*, 1964, **25**, 1–10.
48 R. Miloua, F. Miloua, A. Arbaoui, Z. Kebbab and N. Benramdane, *Solid State Commun.*, 2007, **144**, 5–9.
49 I. Felner and J. Gersten, *Czech J. Phys.*, 1996, **46**, 1421–1422.
50 D. A. Kudryavtsev, B. V. Mill, N. F. Vedernikov and I. S. Shaplygin, *Inorg. Mater.*, 1992, **28**, 943–946.
51 D. DuBoulay, E. N. Maslen, V. A. Streltsov and N. Ishizawa, *Acta Crystallogr., Sect. B: Struct. Sci.*, 1995, **51**, 921–929.
52 L. Miranda, K. Boulahya, A. Varela, J. M. Gonzalez-Calbet, M. Parras, M. Hernando, M. T. Fernandez-Diaz, A. Feteira and D. C. Sinclair, *Chem. Mater.*, 2007, **19**, 3425–3432.
53 H. T. Stokes and D. M. Hatch, *J. Appl. Crystallogr.*, 2005, **38**, 237–238.
54 J. Cui, Q. Huang and B. H. Toby, *Powder Diffr.*, 2006, **21**, 71–79.
55 V. F. Sears, *J. Neutron Res.*, 1992, **3**, 26–37.
56 P. M. Woodward and P. Karen, *Inorg. Chem.*, 2003, **42**, 1121–1129.
57 W. H. Baur, *Acta Crystallogr., Sect. B: Struct. Sci.*, 1974, **30**, 1195–1215.

58 K. Momma and F. Izumi, *J. Appl. Crystallogr.*, 2011, **44**, 1272–1276.
59 H. Saalfeld, *Z. Kristallogr., Mineral. Petrogr., Abt. A*, 1964, **120**, 342–348.
60 A. Munoz, J. A. Alonso, M. J. Martinez-Lope and J. L. Martinez, *Chem. Mater.*, 2004, **16**, 4087–4094.
61 N. Kallel, S. Ben Abdelkhalek, S. Kallel, O. Pena and M. Oumezzine, *J. Alloys Compd.*, 2010, **501**, 30–36.
62 J. H. Shin, M. S. Song and J. Y. Lee, *J. Electroceram.*, 2006, **17**, 205–209.
63 E. García-Matres, J. L. Martínez, J. Rodríguez-Carvajal, J. A. Alonso, A. Salinas-Sánchez and R. Saez-Puche, *J. Solid State Chem.*, 1993, **103**, 322–333.
64 B. H. Toby, *J. Appl. Crystallogr.*, 2001, **34**, 210–213.
65 A. C. Larson and R. B. Von Dreele, *General Structure Analysis System (GSAS)*, 1994.